The Ir-OOOO-Ir Transition State and the Mechanism of the Oxygen Evolution Reaction on IrO 2 (110)

Tobias Binninger, Marie-Liesse Doublet

Journal Name

ARTICLE TYPE

Cite this: DOI: 00.0000/xxxxxxxxxx

The Ir–OOOO–Ir Transition State and the Mechanism of the Oxygen Evolution Reaction on $IrO_2(110)$†

Tobias Binninger,*[a] and Marie-Liesse Doublet[a]

Received Date
Accepted Date

DOI: 00.0000/xxxxxxxxxx

Carefully assessing the energetics along the pathway of the oxygen evolution reaction (OER), our computational study reveals that the "classical" OER mechanism on the (110) surface of iridium dioxide (IrO_2) must be reconsidered. We find that the OER follows a bi-nuclear mechanism with adjacent top surface oxygen atoms as *fixed* adsorption sites, whereas the iridium atoms underneath play an indirect role and maintain their saturated 6-fold oxygen coordination at all stages of the reaction. The oxygen molecule is formed, via an Ir–OOOO–Ir transition state, by association of the outer oxygen atoms of two adjacent Ir–OO surface entities, leaving two intact Ir–O entities at the surface behind. This is drastically different from the commonly considered mono-nuclear mechanism where the O_2 molecule evolves by splitting of the Ir–O bond in an Ir–OO entity. We regard the rather weak reducibility of crystalline IrO_2 as the reason for favoring the novel pathway, which allows the Ir–O bonds to remain stable and explains the outstanding stability of IrO_2 under OER conditions. The establishment of surface oxygen atoms as *fixed* electrocatalytically active sites on a transition-metal oxide represents a paradigm shift for the understanding of water oxidation electrocatalysis, and it reconciles the theoretical understanding of the OER mechanism on iridium oxide with recently reported experimental results from operando X-ray spectroscopy. The novel mechanism provides an efficient OER pathway on a weakly reducible oxide, defining a new strategy towards the design of advanced OER catalysts with combined activity and stability.

Broader Context

The vision of a hydrogen economy is more and more turning into reality after becoming one of the top priorities of industrial policies around the globe. Water electrolysis will likely become the workhorse for the massive generation of clean hydrogen, but the limited energy efficiency of the process is a major obstacle for the industrial upscaling. Whereas the cathodic hydrogen evolution reaction is relatively fast and efficient, the anodic oxygen evolution reaction (OER) is slow and responsible for a significant share of the energy losses, for which reason the OER is in the focus of current electrocatalysis research. Iridium oxide (IrO_2) is the most important OER catalyst in acidic conditions, providing both high activity and stability. Therefore, a thorough understanding of the OER mechanism on IrO_2 is the starting point for the search for cheaper alternatives. Surprisingly, we discovered that the oxygen molecule evolves from the IrO_2 surface in an entirely different way than conventionally assumed, involving an intriguing Ir–OOOO–Ir transition state with a fourfold chain of oxygen atoms. Our findings have a critical impact on our understanding of the OER and reveal a new strategy towards the design of stable and active next-generation OER electrocatalysts.

Introduction

The oxygen evolution reaction (OER) is the kinetic bottleneck of aqueous electrolysis[1], and, as such, of utmost importance for the energy efficiency of the electrochemical production of sustainable hydrogen and chemical feedstock. Iridium oxide provides high electrocatalytic activity towards the OER combined with good stability under acidic OER conditions[2–5], for which reason it is the most important OER electrocatalyst applied in proton-exchange-membrane water electrolyzers. The scarcity and price of iridium, however, is a matter of concern[6] and the development of OER electrocatalysts with reduced noble metal content is a mandate for present electrocatalysis research[7–9]. The detailed investigation of the OER mechanism at an atomistic level is crucial for these efforts and led to the identification of "scaling relations" among the adsorption energies of OER intermediate species[10,11] that provide an explanation for observed volcano-shaped trends in OER activities of various metal oxides and serve as a guide for the discovery of novel electrocatalyst materials[12].

[a] *ICGM, Univ Montpellier, CNRS, ENSCM, Montpellier, France. E-mail: tobias.binninger.science@gmx.de*

† Electronic Supplementary Information (ESI) available: Computed DOS of bulk IrO_2; Pictures of investigated adsorbate configurations at $IrO_2(110)$; Computed grand-canonical stability diagrams; Computed OER pathways including OO energy penalty; Computed grand-canonical free energies of OER intermediate states. See DOI: 00.0000/00000000.

Due to the importance of iridium oxide for OER electrocatalysis, the reaction mechanism on crystalline rutile IrO_2 has attracted considerable interest both from the experimental[5,13–18] and the computational/theoretical[19–26] side, with a particular focus on the $IrO_2(110)$ surface, which has been identified as the thermodynamically stable orientation across a wide potential range[27,28] and generally serves as a reference system for OER electrocatalysis. According to the "classical" OER mechanism proposed by Rossmeisl et al.[19], the O_2 molecule is formed from two H_2O molecules through a sequence of surface-adsorbed intermediate species involving four proton–electron transfer (PET) steps (RS: reaction step),

$$Ir^* + H_2O \rightarrow Ir^*OH + H^+ + e^- \quad \text{(RS1)}$$

$$Ir^*OH \rightarrow Ir^*O + H^+ + e^- \quad \text{(RS2)}$$

$$Ir^*O + H_2O \rightarrow Ir^*OOH + H^+ + e^- \quad \text{(RS3)}$$

$$Ir^*OOH \rightarrow Ir^* + O_2 + H^+ + e^- \quad \text{(RS4)}$$

where Ir^* represents a coordinately unsaturated surface iridium cation that serves as the active adsorption site for the electrocatalytic cycle. The formation of the $^*OOH$ intermediate in (RS3) has been identified as the potential-determining step (PDS), meaning that it is the last step to become downhill in free energy with increasing overpotential[19]. Ping et al.[21] refined (RS3) into the sequence of a "chemical" water dissociation step and a subsequent PET,

$$Ir^*O + Ir^*O + H_2O \rightarrow Ir^*OOH + Ir^*OH \quad \text{(RS5)}$$

$$Ir^*OOH + Ir^*OH \rightarrow Ir^*OO + Ir^*OH + H^+ + e^- \quad \text{(RS6)}$$

where the $^*OOH$ intermediate is oxidized to an $^*OO$ surface adsorbate. The neighboring Ir^*OH gets oxidized in a fourth PET,

$$Ir^*OO + Ir^*OH \rightarrow Ir^*OO + Ir^*O + H^+ + e^- \quad \text{(RS7)}$$

and the oxygen molecule evolves by desorption of the $^*OO$ adsorbate,

$$Ir^*OO \rightarrow Ir^* + O_2 \quad \text{(RS8)}$$

after which the catalytic cycle restarts in (RS1) with the adsorption and deprotonation of a water molecule on the unsaturated Ir^*.

Likewise, in essentially all OER mechanisms discussed to date, coordinately unsaturated transition-metal cations with a formally reduced oxidation state are left behind after the evolution of the oxygen molecule. This not only holds for classical "adsorbate-evolving mechanisms" as discussed above, but also for alternative "lattice oxygen mechanisms" that involve the formation of lattice oxygen vacancies in the surface layer of the metal oxide catalyst[1,29–35]. As a second universal aspect, the first formation of an O–O bond at the metal oxide surface directly produces the OO motif that eventually evolves as an O_2 molecule.

In contrast, our density-functional theory (DFT) computational results strongly suggest that the classical adsorbate-evolving mechanism of the OER on the $IrO_2(110)$ surface does *not* proceed through an O_2 evolving step (RS4) or (RS8) with an unsaturated Ir^* intermediate species. Instead, we demonstrate that the iridium surface atoms remain fully saturated with a 6-fold oxygen coordination at all stages of the OER pathway, and the O_2 molecule evolves in an association step of the outer oxygen atoms of two adjacent Ir^*OO entities via an Ir^*OOOO^*Ir transition state,

$$Ir^*OO + OO^*Ir \xrightarrow{Ir^*OOOO^*Ir} Ir^*O + O_2 + O^*Ir \quad \text{(RS9)}$$

Thus, the OER proceeds entirely on an oxygen-covered surface through two water dissociation sequences (RS5)→(RS6)→(RS7) producing two adjacent Ir^*OO entities, followed by the O_2-evolution step (RS9). The saturated iridium cations are only indirectly involved by creating a redox-active electronic state of the topmost surface oxygen species that act as the fixed sites for adsorption along the OER pathway. Importantly, the novel electrocatalytic cycle involves both the formation and the cleavage of O–O bonds at the top surface oxygen atoms during water dissociation (RS5) and O_2-association (RS9), respectively. Whereas all of the OER mechanisms discussed to date only involve a unidirectional sequence of oxidation steps for the oxygen species up to the finally evolving O_2 molecule, the novel mechanism establishes a *closed redox cycle of fixed surface oxygen species as active centers*, providing an entirely novel design principle for metal-oxide OER catalysts.

Computational Methods

DFT calculations were performed, including spin-polarization, with the VASP package[36] using the PAW method[37] and the PBE[38] GGA exchange-correlation functional. The plane-wave energy cutoff was 520 eV, Fermi-Dirac smearing with $kT = 0.05$ eV was set, and the D3(BJ) method[39] was used to account for dispersion interaction. The PBE functional has been shown to provide an accurate description of the electronic properties of IrO_2[40,41], with the density of states of bulk IrO_2 obtained from our calculations in good agreement, see Supplementary Information (SI) Figure S1. Also the computed tetragonal lattice constants of the relaxed IrO_2 rutile structure (comp.: $a = 4.515$ Å and $c = 3.182$ Å) agree within less than 1% with experimental values[42] (exp.: $a = 4.505$ Å and $c = 3.159$ Å). Symmetric 5-layered $IrO_2(110)$ slabs were constructed from the relaxed bulk structure with the help of the pymatgen python package[43], comprising the 2×1 surface cell of the (110) orientation with 4 iridium atoms per layer. Slab calculations were performed with a Γ-centered $(3 \times 3 \times 1)$ k-point mesh. Atomic positions of all systems were relaxed with a convergence threshold of $0.01\,\text{eV}\,\text{Å}^{-1}$ for the forces, keeping the innermost IrO_2 layer frozen. Periodic slab images were separated by a 20 Å-wide interspace region that was filled with implicit water described by the polarizable continuum model in the VASPsol implementation[44] with a dielectric constant $\varepsilon_r = 78.4$ and using a critical density parameter $n_c = 0.0025\,\text{Å}^{-3}$ to define the implicit solvent boundary. All structural images in the present work were produced using the VESTA software[45].

Water-derived adsorbates were placed symmetrically on both

surfaces of the $IrO_2(110)$ slab (see SI Figures S2 and S3), and free energies were computed according to $A = E_{DFT} + A_{vib}$ from the ground-state DFT energies E_{DFT} by adding the vibrational free energies A_{vib} at $T = 25°C$ of the computed vibrational frequency spectrum in harmonic approximation. The influence of electrochemical interface charging was simulated using the homogeneous background method[46] in a recently developed version[47] for the treatment of electrode surfaces in presence of adsorbate species. In short, the electron number N was varied with respect to N_0 of the neutral cell, and the free energy was transformed to the grand potential $\Omega = A - E_{Fermi}(N - N_0)$ for a potentiostatic setting, where the chemical potential is given by the Fermi energy. The electrode potential $e\mathscr{E} = (-e)\phi_{elyte} - E_{Fermi}$ was determined as the "work function" of the electrode surface in the implicit water environment, where ϕ_{elyte} is the electrostatic potential level in the bulk implicit solvent. A reference value of 4.44 eV was used for the standard hydrogen electrode (SHE) potential[48]. Electrochemical reaction free energies were determined using the computational hydrogen electrode method[49] by referencing the chemical potential of proton–electron pairs at the potential of the reversible hydrogen electrode (RHE) to half the Gibbs free energy per molecule of hydrogen gas. Gibbs free energies $G = H - TS$ of liquid water, gaseous hydrogen and gaseous oxygen at $T = 25°C$ and $p = 1$ bar were computed from the ground-state DFT energies of relaxed H_2O, H_2, and O_2 molecules, respectively, adding the vibrational zero-point energy, as well as the CODATA[50] tabulated values of the corresponding entropic $(-TS)$-contribution, gas-phase enthalpy difference $H(298.15\,K) - H(0\,K)$, and, for liquid water, heat of condensation $H_{H_2O,liq} - H_{H_2O,gas}$ at 298.15 K. The energy of the oxygen molecule is known to be poorly described at the GGA-level[51], for which reason the free energy of gaseous O_2 is commonly determined indirectly from the H_2 and H_2O free energies to yield the correct standard equilibrium potential of $1.229\,V_{SHE}$ for the OER. Using the DFT-derived free energy of O_2, we obtain an equilibrium potential of $1.127\,V_{SHE}$. The difference of 0.102 eV (per electron) could be compensated by an O_2 energy correction of +0.408 eV. However, for the sake of consistency, we prefer to first treat all of O_2, H_2, and H_2O at an equal footing and accept the energetic errors of the computational framework. We then discuss the robustness of our results against such errors by adding +0.408 eV to the O_2 energy, and the same *per OO entity* for all adsorbate states of the $IrO_2(110)$ surface involving such motifs. A similar energy shift has also been previously reported for the PBE functional[21,51].

To validate the computational results in comparison with reported experimental results, cyclic voltammograms (CVs) were simulated in terms of the electrochemical interface capacitance as a function of the electrode potential. For this purpose, we first computed the grand partition function $Z_\Omega = \sum_i \exp(-\Delta\Omega_i/kT)$ from the grand potential curves $\Delta\Omega_i$ of the individual adsorbate configurations, see Figure 1, from which we obtained the total grand potential $\Omega = -kT\log(Z_\Omega)$, see the "concave hull" in Figure 1. Charge and capacitance were then computed from the derivatives of the grand potential with respect to the electrode potential[47,52,53], $Q = -\partial\Omega/\partial\mathscr{E}$ and $C = -\partial^2\Omega/\partial\mathscr{E}^2$.

Activation energy barriers for the relevant reaction steps were

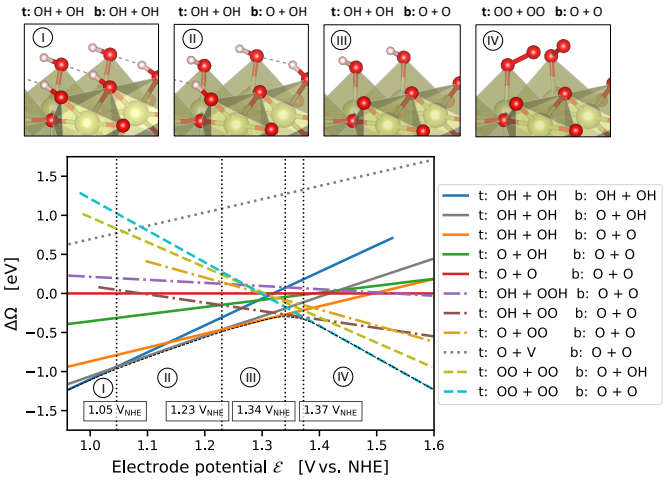

Fig. 1 Computed grand-canonical stability diagram of adsorbate configurations on the $IrO_2(110)$ surface in aqueous environment at pH = 0 with the fully *O-covered surface as reference system. Vertical dotted lines indicate the equilibrium potentials for the transition between lowest-energy adsorbate states (shown above with oxygen: red; hydrogen: white; iridium: pale golden). The total grand potential of the system is the "concave hull", shown as a thin black dashed curve. Naming scheme: Species at the top (t) and bridge (b) oxygen sites (two of each per simulated surface cell); V: Vacant top oxygen site.

obtained from the climbing-image nudged elastic band (CI-NEB) method[54]. The barriers were computed at constant-charge conditions. The treatment of gas-phase entropy contributions in NEB calculations must be carefully assessed. Unlike in Ref.[21], we consider it more consistent to *not* include O_2 gas-phase entropy contributions *at the transition-state* of the oxygen evolution steps. Gas-phase entropy primarily results from the translational degrees of freedom of the "free" gas molecules in the final state. In contrast, the OO entity at the transition state of O_2 evolution does not possess such translational freedom due to its linkage to a specific motif of surface sites from which it evolves. The gas-phase entropy thus only affects the entirely free product state of the evolved O_2 molecule, which has no influence on the forward rate of the elementary reaction step.

Results

Figure 1 presents the computed grand-canonical stability diagram of the relevant aqueous adsorbate configurations on $IrO_2(110)$ at pH = 0. The relative stability and equilibrium potentials between the mixed *O- and *OH-covered surface states are in excellent agreement with previously reported results[21] (see SI Figure S4). Above $1.23\,V_{NHE}$, the bridge oxygen sites are largely deprotonated and remain inactive, while the top sites are fully covered with *OH (labelled (III) in Figure 1). Taking into account adsorbate states with *OOH and *OO entities, we find that the fully protonated top oxygen sites would transform into a completely *OO-covered state (labelled (IV) in Figure 1) around $1.34–1.37\,V_{NHE}$. These qualitative results are robust against the OO energy correction discussed above, which merely shifts the latter transition potential to around $1.5\,V_{NHE}$ as shown in SI Figure S5. It is important to note that, as shown by the dotted curve in Figure 1, the

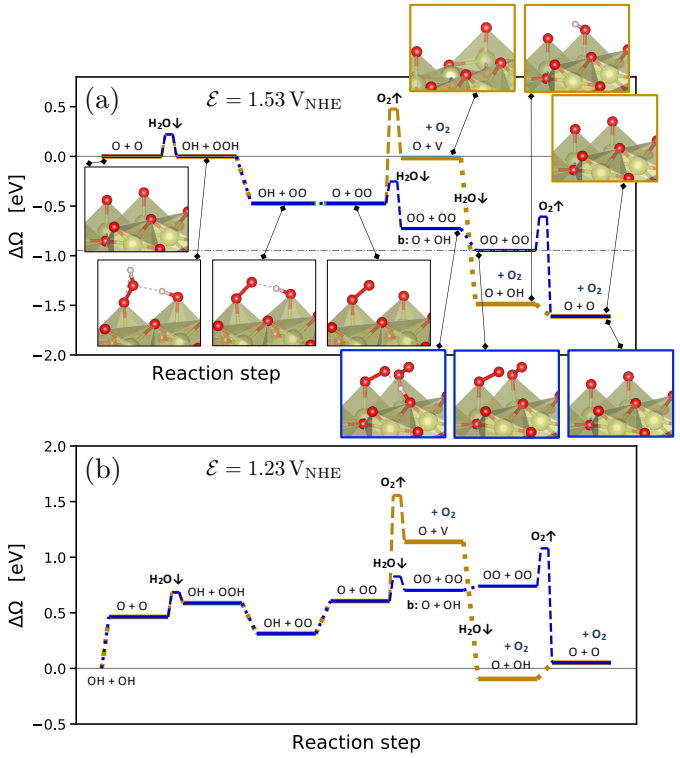

Fig. 2 Comparison between the conventionally considered OER mechanism (golden color) and the novel mechanism (blue color) at pH = 0 and a potential of $1.53\,\mathrm{V_{NHE}}$ (a) and $1.23\,\mathrm{V_{NHE}}$ (b). The intermediate adsorbate configurations are shown and denoted by the occupation of the two top oxygen sites per surface cell. If not otherwise indicated, the bridge oxygen sites are occupied by O + O. Reaction barriers of dissociative water adsorption ($H_2O\downarrow$) and oxygen evolution ($O_2\uparrow$) steps were estimated from climbing-image NEB calculations for the neutral systems, see Figure 3. The zero energy reference was chosen at the respective lowest-energy surface configuration involving only *O and *OH, see Figure 1. The absolute lowest-energy configuration OO + OO at $1.53\,\mathrm{V_{NHE}}$ is indicated by a dash-dotted line in (a). Note that *no* correction of the OO energy was applied, for which reason the initial and final states at the correct equilibrium potential in (b) are slightly misaligned.

state with an oxygen vacancy (V) at the top site, corresponding to an unsaturated Ir* (see SI Figure S2), is thermodynamically out of reach. This is not surprising, because strong dissociative adsorption of water molecules to Ir* is known to occur at the stoichiometric $IrO_2(110)$ surface[21], for which we obtain a binding energy of 1.3 eV per H_2O. However, this observation already indicates that, even if temporary, the formation of unsaturated Ir* in the course of the OER, as in steps (RS4) or (RS8), is rather unlikely.

How then could the O_2 molecule evolve from the surface without creating Ir*? As discussed above, the thermodynamically stable surface configuration in the OER-relevant potential range involves complete coverage of the top oxygen sites by *OO. As shown in the structural drawing (IV) of Figure 1, the spatial extension of the *OO entities enables the outer oxygen atoms of two adjacent *OO to closely interact without requiring distortion of the underlying IrO_2 lattice. We therefore propose reaction (RS9) as the actual O_2-evolution step at the $IrO_2(110)$ surface, where the O_2 molecule is formed by association of the outer oxygen atoms of neighboring *OO while preserving the full coordination of surface Ir cations. Figure 2 compares the novel pathway (blue) with the conventional one (golden) at an OER-relevant electrode potential of $1.53\,\mathrm{V_{NHE}}$ in 2(a) and the equilibrium potential of $1.23\,\mathrm{V_{NHE}}$ in 2(b). The results for the conventional pathway agree very well with previous reports[21]. As expected from the slight error in the computational equilibrium potential discussed above, the initial and final states in 2(b) are not aligned at the real equilibrium potential. Results including the OO energy correction, with aligned initial and final states at $1.23\,\mathrm{V_{NHE}}$, do not affect the conclusion and are shown in SI Figure S7. The grand-canonical free energies of all OER intermediate states shown in Figure 2 are given in SI Tables S1 and S2. The novel mechanism shares the same steps as the conventional one until a top *OO entity is formed. According to the conventional mechanism, this *OO directly evolves as O_2. In the novel mechanism, another adjacent *OO entity is first formed, and the outer oxygen atoms finally associate to evolve as O_2. From the energetic alignment of the respective intermediate states, it becomes directly clear that the novel OER mechanism is favored over the conventional one at any potential. In fact, at $1.53\,\mathrm{V_{NHE}}$ all steps of the novel mechanism are downhill, whereas the O_2 evolution step of the conventional mechanism costs a significant uphill free energy of 0.46 eV.

To estimate the influence of the activation energy barriers, we used the climbing-image nudged elastic band (CI-NEB) method[54] for dissociative water adsorption on the *O-covered surface (RS5), oxygen evolution by *OO–OO* association (RS9) (novel mechanism), and oxygen evolution by desorption (RS8) (conventional mechanism). We assume the barriers of simple PET steps in acidic conditions to be negligible. The corresponding energy barriers are shown in Figure 3 together with images of the initial, final, and intermediate/transition states. The presented results were obtained for the neutral systems, but we also performed NEB calculations at a fixed negative surface charge as discussed below. For the conventional O_2 evolution step by desorption, we obtained an activation energy of $\Delta E_{\mathrm{DFT}} = 0.95\,\mathrm{eV}$, measured with respect to the initial state of a single adsorbed *OO, see Figure 3(c). In contrast, the novel step of O_2 evolution by *OO–OO* association only requires an activation energy of $\Delta E_{\mathrm{DFT}} = 0.34\,\mathrm{eV}$, measured with respect to the ground-state of two adjacent *OO, see Figure 3(b). Therefore, both thermodynamically and kinetically, the novel OER mechanism on $IrO_2(110)$ is favored over the conventional. As shown in SI Figure S7, this conclusion also holds when adding the OO energy penalty discussed above.

The transition state of the O_2 evolution step is an intriguing Ir–OOOO–Ir entity with a chain of four oxygen atoms and three O–O bonds, see Figure 3(b). The evolving O_2 molecule results from creating a novel inner O–O bond while splitting the two outer O–O bonds, whereas the basal Ir–O bonds remain intact. The creation of the O–O bond of the evolving O_2 molecule is shown in Figure 4 at the Ir–OOOO–Ir state, where all three O–O bonds have an equal length of 1.44 Å, indicating peroxide-type bonding. Figure 4(c) shows the σ-bonding charge density of the newly forming inner O–O bond, which becomes visible in the local density of states (LDOS) integrated over the energy range from −3.0 to −2.0 eV vs. E_{Fermi}. In the energy range from −2.0 to

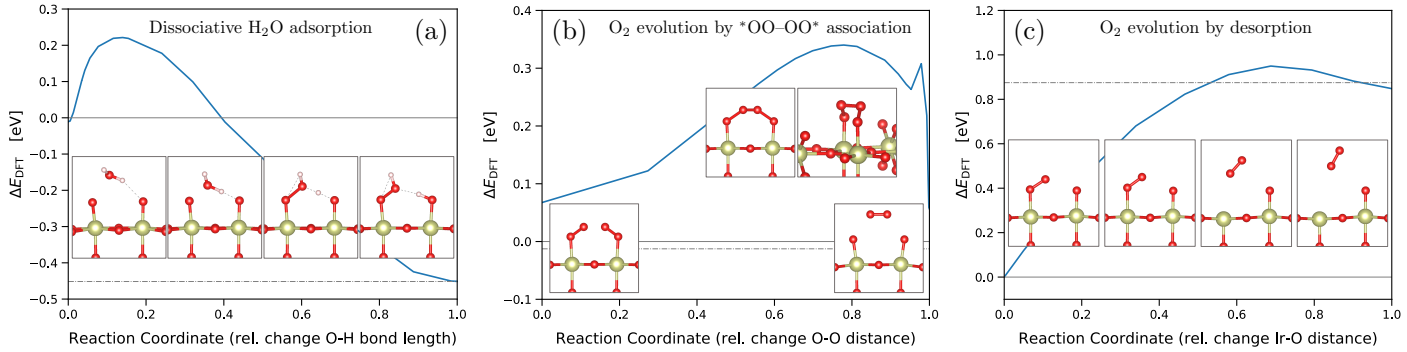

Fig. 3 Activation energy barriers from climbing-image NEB[54] calculations for dissociative water adsorption on the *O covered surface (a), see reaction (RS5), oxygen evolution by *OO–OO* association (b), see reaction (RS9), and oxygen evolution by desorption (c), see reaction (RS8). Initial and final state energies are indicated by horizontal solid and dash-dotted lines, respectively. NEB calculations were performed for uncharged systems.

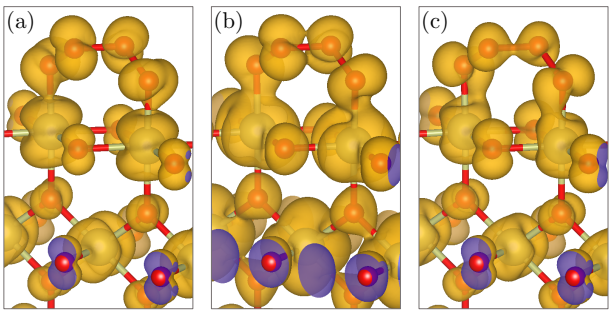

Fig. 4 Creation of the final O–O bond of the evolving O_2 molecule at the Ir–OOOO–Ir transition state: Isosurface plots of the local density of states (LDOS) integrated over different energy ranges (PARCHG file from VASP): (a) from -1.0 to 0.0 eV vs. E_{Fermi}, (b) from -2.0 to -1.0 eV vs. E_{Fermi}, and (c) from -3.0 to -2.0 eV vs. E_{Fermi}.

-1.0 eV vs. E_{Fermi}, we observe certain π-bonding characteristics, see Figure 4(b), whereas the LDOS in the energy range directly below the Fermi level reveals a π^*-antibonding character, see Figure 4(a). We further note that the LDOS plots also show the crystal-field splitting of the iridium 5*d* orbitals. The shape of the LDOS around the iridium atom of the second layer in Figure 4(a) (at the lower-half center) results from the superposition of the d_{xz} and d_{yz} orbitals that determine the density of states around the Fermi level, whereas the $d_{x^2-y^2}$ orbital dominates in the energy range from -2.0 to -1.0 eV vs. E_{Fermi}, shown in Figure 4(b). In the range from -3.0 to -2.0 eV vs. E_{Fermi}, all three orbitals d_{xz}, d_{yz}, and $d_{x^2-y^2}$ have approximately equal contributions, resulting in the t_{2g}-like LDOS visible in Figure 4(c). The t_{2g}-like iridium 5*d* orbitals are involved in π-type Ir–O interactions. These observations are in very good agreement with previously reported results for the crystal-field splitting and bonding in bulk IrO_2[40].

The question remains for the rate-determining step (RDS) of the novel OER mechanism. The dissociative H_2O adsorption on the *O-covered surface has been identified as RDS of the conventional mechanism[21]. However, in this study, the O_2-desorption barrier had been lowered by adding entropy contributions of the free O_2 molecule to the transition state. As discussed in the Computational Methods section, we consider it more consistent with transition-state theory to relate the transition state to the initial state rather than the final state of the given elementary step. Without including the final-state entropy contribution, the O_2-desorption barrier of $\Delta E_{\mathrm{DFT}} = 0.95$ eV is significantly higher than the H_2O-dissociation barrier, for which we obtained $\Delta E_{\mathrm{DFT}} = 0.22$ eV, see Figure 3(a), at the uncharged *O-covered surface (with a potential of zero charge of $2.59\,V_{\mathrm{SHE}}$). Although H_2O dissociation according to reaction (RS5) could be regarded as a "chemical" step due to the absence of PET, Ping et al.[21] found a marked potential dependence of the corresponding energy barrier. We therefore also performed a NEB calculation for the charged system with a constant excess surface charge of $-0.6\,\mathrm{e\,nm^{-2}}$, corresponding to an electrode potential of $1.69\,V_{\mathrm{SHE}}$ for the *O-covered surface in the initial state. Under these conditions, we obtained an H_2O-dissociation barrier of $\Delta E_{\mathrm{DFT}} = 0.55$ eV, significantly larger than for the neutral system, and in good agreement with the previously reported values at similar potentials[21]. However, even when taking into account the influence of surface charging, the H_2O-dissociation barrier remains significantly smaller than the energy barrier of the conventional O_2-desorption step, so that the latter would be rate-limiting for the conventional OER mechanism. For the energy barrier of the novel O_2-evolution step by *OO–OO* association, we found a negligible dependence on the charge state of the surface ($\Delta E_{\mathrm{DFT}} = 0.33$ eV at $-0.6\,\mathrm{e\,nm^{-2}}$ vs. $\Delta E_{\mathrm{DFT}} = 0.34$ eV for the uncharged system). From the comparison with the H_2O-dissociation barrier, we conclude that H_2O dissociation according to reaction (RS5) is the RDS of the novel OER mechanism on $IrO_2(110)$ in the OER-relevant potential range. Close to the OER equilibrium potential, however, the thermodynamic destabilization of the *OO-covered surface state compared to the *O-covered state can make the Ir–OOOO–Ir transition state of the O_2-evolution step the highest point to be overcome along the free-energy profile of the OER pathway, see Figure 2(b).

Discussion

Given the extensive research in the field of OER electrocatalysis during the past decade, we acknowledge that the proposition of a major change in the "classical" mechanism on IrO_2 might appear surprising. We emphasize that both our computational methodology and our results agree in all relevant aspects with the state of

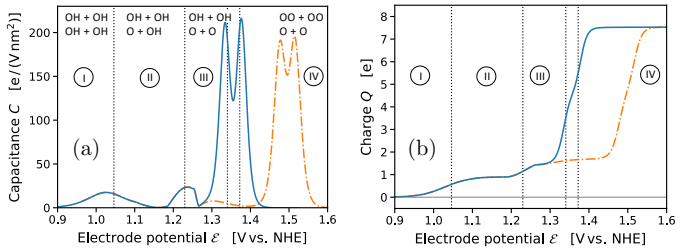

Fig. 5 Computed cyclic voltammogram (a) of an $IrO_2(110)$ electrode at pH = 0, and integrated charge (b) per 2×1 surface cell with the fully *OH-covered surface (**t:** OH + OH **b:** OH + OH) as zero-charge reference state. The results including the OO energy penalty are shown as dash-dotted curves. Vertical dotted lines and numbered potential ranges have the same meaning as in Figure 1. The most stable adsorbate configurations in the respective potential ranges are indicated with top and bridge occupations.

the art[21]. We therefore attribute the discovery of the novel mechanism simply to it having been overlooked so far, rather than any difference in methodology. In the following, we show that the novel OER pathway is strongly supported by the current experimental state of knowledge.

We first compare the cyclic voltammogram (CV) derived from our results with the experimental CV reported for the same system[16]. The computed CV of the $IrO_2(110)$ electrode at pH = 0 is plotted in Figure 5(a) in terms of the capacitance C as a function of the electrode potential $\mathscr{E}$, see Computational Methods. The respective results including the OO energy correction are shown as dash-dotted curves. The computed CV is characterized by two broad pseudocapacitive peaks in the potential range 1.0–1.3 V_{NHE} that correspond to the deprotonation of the two bridge oxygen sites of the simulated 2×1 surface cell, see Figure 1. These features are in agreement with the broad pseudocapacitive region observed in the experimental CV of $IrO_2(110)$ in acidic electrolyte within the same potential range, as reported by Kuo et al.[16]. Also the integrated charge, shown in Figure 5(b), agrees well with the experimental results. The plateau in the charge plot around 1.3–1.4 V_{NHE} (before the final steep increase) corresponds to a charge of 1.6–1.7 electrons per 2×1 surface cell, which is in excellent agreement with a reported value of around 1.7 (0.85 electrons per surface top-site Ir)[16]. We conclude that the pseudocapacitive pre-OER region in the CV of $IrO_2(110)$ corresponds to the deprotonation of bridge oxygen sites, in agreement with the spectroscopic observation of the formation of "O^{I-}" species within the same potential range reported by Saveleva et al.[18], which the authors assigned to deprotonated bridge oxygen species. However, based on our analysis, this process has no direct relation to the OER, because the bridge oxygen are "spectator" species during the OER cycle. The OER-relevant top oxygen sites are passivated due to protonation in the pre-OER region.

The formation of the OER-active state of the top oxygen species occurs in the pronounced peak of the simulated CV between 1.3–1.4 V_{NHE}, which, including the OO energy correction, shifts to the range 1.45–1.55 V_{NHE}, in excellent agreement with the experimental OER onset on $IrO_2(110)$ in acidic electrolyte[16]. Thermodynamically, the top oxygen state would transform from protonated *OH straight to *OO, see Figure 1. However, the OER drives the surface out of equilibrium in this potential range, and the surface state becomes dependent on the kinetics and RDS of the OER mechanism. We argued that the O_2-desorption step would be rate-limiting for the conventionally considered mechanism, with a significantly larger activation energy than the H_2O-dissociation step. In such a case, the *OOH and *OO intermediates would equilibrate with all "upstream" species of the OER pathway, in particular the *OH and *O surface states, and the top surface sites would become fully covered with *OO, see Figure 1. The same would hold for the novel mechanism if the O_2-evolution step (RS9) was rate-limiting. However, we saw from the NEB calculations that at OER-relevant potentials the formation of *OOH in the H_2O-dissociation step (RS5) is more likely the RDS of the novel mechanism, so that the surface state equilibrates primarily among the upstream species of *OH and *O. This would result in a dominant *O-coverage in the OER potential range above 1.5 V_{NHE}, see SI Figure S4, in agreement with the spectroscopic findings by Pedersen et al.[55]. The *OOH and *OO entities lie "downstream" of the RDS towards the OER product side, resulting in a low, kinetically controlled surface coverage, for which reason the spectroscopic detection of such species[56] is challenging.

Different studies have highlighted the central role of electrophilic surface oxygen atoms with a certain radical character[18,21,26,57,58] for the OER mechanism on iridium oxides. Based on the spectroscopic observation of "O^{I-}" species, Pfeifer et al.[58] and Saveleva et al.[18] have suggested an oxygen-anion redox cycle, in contrast to the conventional notion of a transition-metal-cation redox cycle. However, none of the proposed OER mechanisms to date is consistent with such a perspective, because, even if temporarily in an "O^{I-}" state, the active surface oxygen species follow a *unidirectional oxidation* sequence until they become part of the evolving O_2 molecule. Furthermore, the existence of coordinately unsaturated Ir* species after the O_2-evolution step is implied in any of these mechanisms, so that the actual redox *cycle* is provided by iridium cations rather than surface oxygen anions. The novel OER mechanism closes this consistency gap by establishing a *fully closed anion redox cycle* of top surface oxygen species on $IrO_2(110)$ that represent the fixed adsorption sites along the OER pathway. The Ir cations underneath the top oxygen sites preserve their full oxygen coordination at all stages and thus only indirectly participate in the OER mechanism. As a consequence, the saturated Ir species merely undergo screened, indirect changes of their oxidation state. In particular, the novel mechanism does not involve partially reduced "Ir^{III+}" species (corresponding to Ir*) at any stage. These findings explain the spectroscopically observed constancy of the iridium oxidation state and the absence of iridium cation species in a reduced oxidation state during OER on IrO_2[18,55]. The novel mechanism thus completes the paradigm shift away from a metal-cation redox cycle to an oxygen-anion redox cycle as the key element of OER electrocatalysis on crystalline iridium oxide, with possible consequences also for other metal oxide catalysts. The suppression of the conventional O_2-desorption step indicates a rather weak reducibility of crystalline IrO_2. In other words, it is a certain resis-

tance of IrO_2 against reduction that favors the novel OER mechanism over the conventional one. This conclusion is supported by the fact that besides rutile-structure IrO_2, *no* other binary oxides of Ir are known, in particular no reduced binary oxide like, e.g., Ir_2O_3 [59]. The novel mechanism provides an efficient pathway for the OER to proceed at the oxygen-covered surface of a weakly reducible oxide. We consider this insight to be of fundamental importance for strategies towards the discovery of advanced metal-oxide-based OER catalysts.

As a unique feature, the novel mechanism involves both the formation and the cleavage of O–O bonds. In fact, it is the splitting of the O–O bond in the Ir^*OO entities during the O_2-evolution step (RS9) which closes the redox cycle of the oxygen species in the remaining Ir^*O entities. The electronic character of the stable top oxygen species must therefore not only enable a facile formation of an O–O bond by water nucleophilic attack in step (RS5), but also a facile splitting of this bond in the subsequent O_2-evolution step (RS9). This aspect is highly relevant for an analysis of scaling relations and volcano-plots [10,11,19,20,60] that typically employ the adsorption energies of $^*OH$, $^*O$, and $^*OOH$ intermediates on coordinately unsaturated transition metal atoms as descriptors. According to the novel mechanism, however, the Ir–O bond of the top Ir^*O entities never gets broken. Instead, it is the adsorption energies of H, OH, and O *on the fixed top oxygen atoms* that govern the energetics along the OER pathway, while the strength of the Ir–O bond only plays an indirect role. Moreover, since the novel OER mechanism does *not* require the breakage of an Ir–O bond, it decouples OER kinetics from metal oxide stability, which is determined by the strength of the Ir–O bond. This explains why high OER activity can be combined with catalyst stability for the case of crystalline IrO_2 [5]. It is interesting to note that mixed-metal-oxide catalysts, such as La_2LiIrO_6/La_2IrO_6, which contain iridium cations in a higher formal oxidation state up to Ir^{VI+}, involve an iridium-cation redox cycle with the formation of oxygen vacancies during OER, resulting in structural decomposition of the catalyst [57]. In contrast, the stable oxygen-anion redox cycle on the weakly reducible IrO_2 enables the unique combination of OER activity and structural stability. The combination of an only weak reducibility of the bulk oxide with an electrophilic oxygen surface termination thus appears a promising principle for the design and discovery of advanced OER catalysts providing both superior activity and stability.

Finally, our findings could also have consequences for the discovery of novel electrocatalyst materials for the oxygen reduction reaction (ORR). We established the deprotonated $^*O$-covered $IrO_2(110)$ surface as the *stable* active state of the electrocatalyst during OER. By reversing the direction of the novel OER mechanism, it appears possible, at least in principle, to design electrocatalysts for the reverse ORR that operate in the oxidized surface state. This could enable higher operation potentials than conventional ORR catalysts, which require reduced transition-metal sites to be available.

Conclusions

In summary, we found that the "classical" OER mechanism on $IrO_2(110)$ proceeds differently than presently assumed. Instead of the conventionally considered O_2-desorption step, the O_2 molecule evolves in an association step from two neighboring Ir^*OO entities via an intriguing Ir^*OOOO^*Ir transition state. At practical OER potentials, the dissociative water adsorption at the $^*O$-covered surface is the rate-determining step, but close to the equilibrium potential, the availability of Ir^*OO surface motifs for the O_2-evolution step becomes the overall thermodynamic bottleneck along the OER pathway. The fixed top oxygen atoms at the $IrO_2(110)$ surface are the active sites of the catalytic cycle, and the surface iridium atoms remain fully coordinated at all stages. The novel mechanism thus corresponds to a fully closed oxygen-anion redox cycle, representing a paradigm shift in OER electrocatalysis and consistently explaining recently reported results from in situ/operando X-ray spectroscopy experiments. Furthermore, our results provide an explanation for the surprising combination of activity and stability for crystalline IrO_2, because the OER occurs without requiring the breaking of Ir–O bonds. Optimizing the strength of the metal–oxygen bond for stability therefore does *not* necessarily jeopardize the OER activity, which is highly relevant for the design of advanced OER catalysts combining performance in both activity and stability.

Conflicts of interest

There are no conflicts to declare.

Acknowledgements

T.B. acknowledges financial support in the form of a research fellowship grant funded by the SNSF (Swiss National Science Foundation).

Notes and references

1 E. Fabbri and T. J. Schmidt, *ACS Catalysis*, 2018, **8**, 9765–9774.
2 C. C. L. McCrory, S. Jung, J. C. Peters and T. F. Jaramillo, *Journal of the American Chemical Society*, 2013, **135**, 16977–16987.
3 N. Danilovic, R. Subbaraman, K.-C. Chang, S. H. Chang, Y. J. Kang, J. Snyder, A. P. Paulikas, D. Strmcnik, Y.-T. Kim, D. Myers, V. R. Stamenkovic and N. M. Markovic, *The Journal of Physical Chemistry Letters*, 2014, **5**, 2474–2478.
4 S. Cherevko, S. Geiger, O. Kasian, N. Kulyk, J.-P. Grote, A. Savan, B. R. Shrestha, S. Merzlikin, B. Breitbach, A. Ludwig and K. J. Mayrhofer, *Catalysis Today*, 2016, **262**, 170–180.
5 T. Weber, V. Vonk, D. Escalera-López, G. Abbondanza, A. Larsson, V. Koller, M. J. Abb, Z. Hegedüs, T. Bäcker, U. Lienert, G. S. Harlow, A. Stierle, S. Cherevko, E. Lundgren and H. Over, *ACS Catalysis*, 2021, **11**, 12651–12660.
6 C. Minke, M. Suermann, B. Bensmann and R. Hanke-Rauschenbach, *International Journal of Hydrogen Energy*, 2021, **46**, 23581–23590.
7 I. Katsounaros, S. Cherevko, A. R. Zeradjanin and K. J. J.

Mayrhofer, *Angewandte Chemie International Edition*, 2014, **53**, 102–121.
8 V. R. Stamenkovic, D. Strmcnik, P. P. Lopes and N. M. Markovic, *Nature Materials*, 2017, **16**, 57–69.
9 C. W. Song, J. Lim, H. B. Bae and S.-Y. Chung, *Energy Environ. Sci.*, 2020, **13**, 4178–4188.
10 I. C. Man, H.-Y. Su, F. Calle-Vallejo, H. A. Hansen, J. I. Martínez, N. G. Inoglu, J. Kitchin, T. F. Jaramillo, J. K. Nørskov and J. Rossmeisl, *ChemCatChem*, 2011, **3**, 1159–1165.
11 M. Busch, N. B. Halck, U. I. Kramm, S. Siahrostami, P. Krtil and J. Rossmeisl, *Nano Energy*, 2016, **29**, 126–135.
12 K. S. Exner, *ACS Applied Energy Materials*, 2019, **2**, 7991–8001.
13 Y. Lee, J. Suntivich, K. J. May, E. E. Perry and Y. Shao-Horn, *The Journal of Physical Chemistry Letters*, 2012, **3**, 399–404.
14 H. G. Sanchez Casalongue, M. L. Ng, S. Kaya, D. Friebel, H. Ogasawara and A. Nilsson, *Angewandte Chemie International Edition*, 2014, **53**, 7169–7172.
15 K. A. Stoerzinger, L. Qiao, M. D. Biegalski and Y. Shao-Horn, *The Journal of Physical Chemistry Letters*, 2014, **5**, 1636–1641.
16 D.-Y. Kuo, J. K. Kawasaki, J. N. Nelson, J. Kloppenburg, G. Hautier, K. M. Shen, D. G. Schlom and J. Suntivich, *Journal of the American Chemical Society*, 2017, **139**, 3473–3479.
17 O. Kasian, J.-P. Grote, S. Geiger, S. Cherevko and K. J. J. Mayrhofer, *Angewandte Chemie International Edition*, 2018, **57**, 2488–2491.
18 V. A. Saveleva, L. Wang, D. Teschner, T. Jones, A. S. Gago, K. A. Friedrich, S. Zafeiratos, R. Schlögl and E. R. Savinova, *The Journal of Physical Chemistry Letters*, 2018, **9**, 3154–3160.
19 J. Rossmeisl, Z.-W. Qu, H. Zhu, G.-J. Kroes and J. Nørskov, *Journal of Electroanalytical Chemistry*, 2007, **607**, 83–89.
20 Z. Xu, J. Rossmeisl and J. R. Kitchin, *The Journal of Physical Chemistry C*, 2015, **119**, 4827–4833.
21 Y. Ping, R. J. Nielsen and W. A. Goddard, *Journal of the American Chemical Society*, 2017, **139**, 149–155.
22 J. A. Gauthier, C. F. Dickens, L. D. Chen, A. D. Doyle and J. K. Nørskov, *The Journal of Physical Chemistry C*, 2017, **121**, 11455–11463.
23 L. G. V. Briquet, M. Sarwar, J. Mugo, G. Jones and F. Calle-Vallejo, *ChemCatChem*, 2017, **9**, 1261–1268.
24 K. S. Exner and H. Over, *ACS Catalysis*, 2019, **9**, 6755–6765.
25 H. N. Nong, L. J. Falling, A. Bergmann, M. Klingenhof, H. P. Tran, C. Spöri, R. Mom, J. Timoshenko, G. Zichittella, A. Knop-Gericke, S. Piccinin, J. Pérez-Ramírez, B. R. Cuenya, R. Schlögl, P. Strasser, D. Teschner and T. E. Jones, *Nature*, 2020, **587**, 408–413.
26 D. González, J. Heras-Domingo, M. Sodupe, L. Rodríguez-Santiago and X. Solans-Monfort, *Journal of Catalysis*, 2021, **396**, 192–201.
27 Y. Ping, W. A. Goddard and G. A. Galli, *Journal of the American Chemical Society*, 2015, **137**, 5264–5267.
28 F. Nattino and N. Marzari, *Phys. Chem. Chem. Phys.*, 2020, **22**, 10807–10818.
29 C. Spöri, J. T. H. Kwan, A. Bonakdarpour, D. P. Wilkinson and P. Strasser, *Angewandte Chemie International Edition*, 2017, **56**, 5994–6021.
30 A. Grimaud, O. Diaz-Morales, B. Han, W. T. Hong, Y.-L. Lee, L. Giordano, K. A. Stoerzinger, M. T. M. Koper and Y. Shao-Horn, *Nature Chemistry*, 2017, **9**, 457–465.
31 O. Kasian, S. Geiger, T. Li, J.-P. Grote, K. Schweinar, S. Zhang, C. Scheu, D. Raabe, S. Cherevko, B. Gault and K. J. J. Mayrhofer, *Energy Environ. Sci.*, 2019, **12**, 3548–3555.
32 K. Schweinar, B. Gault, I. Mouton and O. Kasian, *The Journal of Physical Chemistry Letters*, 2020, **11**, 5008–5014.
33 A. Zagalskaya, I. Evazzade and V. Alexandrov, *ACS Energy Letters*, 2021, **6**, 1124–1133.
34 N. Zhang and Y. Chai, *Energy Environ. Sci.*, 2021, **14**, 4647–4671.
35 S. Czioska, A. Boubnov, D. Escalera-López, J. Geppert, A. Zagalskaya, P. Röse, E. Saraçi, V. Alexandrov, U. Krewer, S. Cherevko and J.-D. Grunwaldt, *ACS Catalysis*, 2021, **11**, 10043–10057.
36 G. Kresse and J. Furthmüller, *Computational Materials Science*, 1996, **6**, 15 – 50.
37 G. Kresse and D. Joubert, *Phys. Rev. B*, 1999, **59**, 1758–1775.
38 J. P. Perdew, K. Burke and M. Ernzerhof, *Phys. Rev. Lett.*, 1996, **77**, 3865–3868.
39 S. Grimme, J. Antony, S. Ehrlich and H. Krieg, *The Journal of Chemical Physics*, 2010, **132**, 154104.
40 J. M. Kahk, C. G. Poll, F. E. Oropeza, J. M. Ablett, D. Céolin, J.-P. Rueff, S. Agrestini, Y. Utsumi, K. D. Tsuei, Y. F. Liao, F. Borgatti, G. Panaccione, A. Regoutz, R. G. Egdell, B. J. Morgan, D. O. Scanlon and D. J. Payne, *Phys. Rev. Lett.*, 2014, **112**, 117601.
41 Y. Ping, G. Galli and W. A. Goddard, *The Journal of Physical Chemistry C*, 2015, **119**, 11570–11577.
42 A. A. Bolzan, C. Fong, B. J. Kennedy and C. J. Howard, *Acta Crystallographica Section B*, 1997, **53**, 373–380.
43 S. P. Ong, W. D. Richards, A. Jain, G. Hautier, M. Kocher, S. Cholia, D. Gunter, V. L. Chevrier, K. A. Persson and G. Ceder, *Computational Materials Science*, 2013, **68**, 314–319.
44 K. Mathew, R. Sundararaman, K. Letchworth-Weaver, T. A. Arias and R. G. Hennig, *The Journal of Chemical Physics*, 2014, **140**, 084106.
45 K. Momma and F. Izumi, *Journal of Applied Crystallography*, 2011, **44**, 1272–1276.
46 J.-S. Filhol and M. Neurock, *Angewandte Chemie International Edition*, 2006, **45**, 402–406.
47 A. Hagopian, M.-L. Doublet, J.-S. Filhol and T. Binninger, *submitted*, preprint: `http://arxiv.org/abs/2201.04537`, 2022.
48 *IUPAC. Compendium of Chemical Terminology, 2nd ed. (the "Gold Book")*, ed. A. D. McNaught and A. Wilkinson, Blackwell Scientific Publications, Oxford, 1997.
49 J. K. Nørskov, J. Rossmeisl, A. Logadottir, L. Lindqvist, J. R. Kitchin, T. Bligaard and H. Jónsson, *The Journal of Physical Chemistry B*, 2004, **108**, 17886–17892.
50 J. D. Cox, D. D. Wagman and V. A. Medvedev, *CODATA Key Val-*

ues for Thermodynamics, Hemisphere Publishing Corp., New York, 1989.

51 E. Sargeant, F. Illas, P. Rodríguez and F. Calle-Vallejo, *Journal of Electroanalytical Chemistry*, 2021, **896**, 115178.

52 W. Schmickler and E. Santos, *Interfacial Electrochemistry*, Springer, Berlin, Heidelberg, 2010.

53 N. G. Hörmann, O. Andreussi and N. Marzari, *The Journal of Chemical Physics*, 2019, **150**, 041730.

54 G. Henkelman, B. P. Uberuaga and H. Jónsson, *The Journal of Chemical Physics*, 2000, **113**, 9901–9904.

55 A. F. Pedersen, M. Escudero-Escribano, B. Sebok, A. Bodin, E. Paoli, R. Frydendal, D. Friebel, I. E. L. Stephens, J. Rossmeisl, I. Chorkendorff and A. Nilsson, *The Journal of Physical Chemistry B*, 2018, **122**, 878–887.

56 N. Sivasankar, W. W. Weare and H. Frei, *Journal of the American Chemical Society*, 2011, **133**, 12976–12979.

57 A. Grimaud, A. Demortière, M. Saubanère, W. Dachraoui, M. Duchamp, M.-L. Doublet and J.-M. Tarascon, *Nature Energy*, 2016, **2**, 16189.

58 V. Pfeifer, T. E. Jones, J. J. Velasco Vélez, R. Arrigo, S. Piccinin, M. Hävecker, A. Knop-Gericke and R. Schlögl, *Chemical Science*, 2017, **8**, 2143–2149.

59 M.-S. Miao and R. Seshadri, *Journal of Physics: Condensed Matter*, 2012, **24**, 215503.

60 M. Busch, *Current Opinion in Electrochemistry*, 2018, **9**, 278–284.